J. Fluid Mech. (2005), *vol.* 529, *pp.* 173–193.
doi:10.1017/S0022112005003356 Printed in the United Kingdom

Infiltration into inclined fibrous sheets

By M. LANDERYOU[1], I. EAMES[2] AND A. COTTENDEN[1]

[1]Department of Medical Physics, University College London, Torrington Place, London WC1E 7JE, UK
[2]Department of Mechanical Engineering and Mathematics, University College London, Torrington Place, London WC1E 7JE, UK

(Received 2 June 2004 and in revised form 30 September 2004)

The flow from line and point sources through an inclined fibrous sheet is studied experimentally and theoretically for wicking from a saturated region and flow from a constant-flux source. Wicking from a saturated line generates a wetted region whose length grows diffusively, linearly or tends to a constant, depending on whether the sheet is horizontal or inclined downwards or upwards. A constant-flux line source generates a wetted region which ultimately grows linearly with time, and is characterized by a capillary fringe whose thickness depends on the relative strength of the source, gravitational and capillary forces. Good quantitative agreement is observed between experiments and similarity solutions.

Capillary-driven and constant-flux source flows issuing from a point on a horizontal sheet generate a wetted patch whose radius grows diffusively in time. The flow is characterized by the relative strength of the source and spreading induced by the action of capillary forces, γ. As γ increases, the fraction of the wetted region which is saturated increases. Wicking from a saturated point corresponds to $\gamma = \gamma_c$, and spreads at a slower rate than from a line source. For $\gamma < \gamma_c$, the flow is partially saturated everywhere. Good agreement is observed between measured moisture profiles, rates of spreading, and similarity solutions.

Numerical solutions are developed for point sources on inclined sheets. The moisture profile is characterized by a steady region circumscribed by a narrow boundary layer across which the moisture content rapidly changes. An approximate analytical solution describes the increase in the size of the wetted region with time and source strength; these conclusions are confirmed by numerical calculations. Experimental measurements of the downslope length are observed to be slightly in excess of theoretical predictions, though the dependence on time, inclination and flow rate obtained theoretically is confirmed. Experimental measurements of cross-slope width are in agreement with numerical results and solutions for short and long times. The effect of a percolation threshold is observed to ultimately arrest cross-slope transport, placing a limitation on the long-time analysis.

1. Introduction

Fibrous sheets are widely used for the absorption of fluids in the health sector, for example in wound dressings, sanitary protection, and incontinence products (Dutkiewicz 2003). Medical absorbents are often complex, having multi-layered structures of varying geometry; disposable products often additionally include super-absorbent polymers. The simplest class of these products is reusable bedpads, which are large homogeneous rectangular fibrous sheets backed by an impermeable layer. Despite the general nature and widespread use of such products, leakage is surprisingly

common (Norris & Cottenden 1993). The distribution process within an incontinence product begins with liquid being introduced into the material under pressure for a short time. This is followed by a longer period during which capillary and gravitational forces dominate to determine liquid distribution and storage within the material. In order to understand how such products function, we need to first address the more general problem of how fluid spreads in homogeneous fibrous sheets, and this forms the basis of this paper.

Capillary forces play an important role in controlling liquid distribution within fibrous and porous materials. The most common example of flow in a fibrous medium can be found in candles where the vertical transport of wax from a molten reservoir, through the wick, feeds the candle flame. The rate of wicking from a reservoir can be used as a measure of the capillary transport potential of a textile (Harnett & Mehta 1984). Liquid spreading through textiles is also important in industrial processes such as resin impregnation in fibrous mats (Pillai & Advani 1996). Transport through porous materials such as soils has been studied much more extensively than spreading in fibrous sheets, particularly in the context of groundwater systems. Motivated by understanding the recharge of groundwater by rain, the problem of a constant line (and point) flux issuing onto a porous material and driven vertically downwards by gravity has been studied theoretically, experimentally and in the field many times.

A starting point for interpreting and modelling infiltration into porous media is through Washburn's (1921) and Richards' (1931) models. Richards' analysis, which we describe in § 2, is based on an analogy with Darcy flow, and requires empirical relations to close the system of equations. While Richards' equation has been applied to a wide variety of practical problems, it has only been used in a few instances to describe flow in thin fibrous sheets (see for example Chaterjee & Gupta 2002). Using closure relations drawn from soil physics, Eames *et al.* (2003) studied numerically the flow from a weak point source on an inclined fibrous sheet, in which the material did not become saturated. This problem is revisited here and studied numerically, theoretically and experimentally, using empirically determined closure relations.

Motivated by the two spreading phases observed for medical absorbents – source-driven flow at the early stages of absorption and later distribution dominated by capillary forces – we focus on two separate driving mechanisms: the flow generated by fluid introduced at a constant rate, and wicking by capillary action from a region maintained at saturation. The challenge is to determine closure relations which permit a bulk description of the transport processes to be calculated. While such closure relations have been developed for different soil types (for example Brooks & Corey 1966; Van Genuchten 1980), they are less common or absent for fabrics. Since the particular mode of transport may be sensitive to these empirical closures, they must be determined before addressing more general problems. A careful choice of closures enables Richards' equation to be solved analytically in some instances. Comparisons are made with experimental measurements of spreading in thin sheets.

The paper is structured as follows. In § 2 we briefly review two modelling approaches for describing flow in fibrous sheets, Washburn's and Richards' models. The closure relations for Richards' equation for a typical fibrous material used in medical absorbents are determined in § 3. In § 4 and § 5 we describe analytical and numerical solutions for line and point sources respectively, which are tested against experimental measurements. The general conclusions are described in § 6.

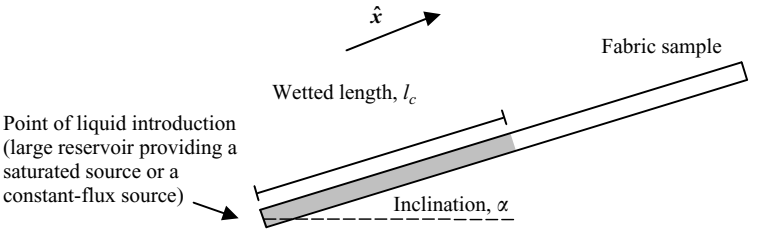

FIGURE 1. Sketch to illustrate the arrangement of a thin fabric sheet at inclination α. Liquid is introduced into the sample as illustrated, with a line source leading to the development of a wetted region of length l_c.

2. Review of modelling approaches

2.1. *Washburn's model*

Washburn's description is often applied to capillary-driven flow from saturated reservoirs in textiles (Kissa 1996). Figure 1 shows an inclined fabric sample with liquid being introduced at one end. Washburn's model of infiltration in such a situation is based on a simplified description, in which the pore space is described as an assembly of small parallel tubes. Physically, the flow is driven from a saturated region (with zero pressure head) by a capillary pressure of magnitude Ψ^*. The flow is resisted by gravity and a viscous shear stress exerted by the tube walls. In combination, the filtration velocity in the medium, $\boldsymbol{u}$, is

$$\boldsymbol{u} = -K_s[\nabla\Psi + \rho g \sin\alpha \hat{\boldsymbol{x}}], \tag{2.1}$$

where Ψ is the pressure, ρ is the density of the flowing liquid, g is gravitational acceleration, α is the inclination of the tube, K_s is the saturated permeability and $\hat{\boldsymbol{x}}$ is a unit vector (shown in figure 1).

Integrating the momentum equation from the reservoir to the contact line, over a distance l_c, yields

$$\int_0^{l_c} \boldsymbol{u}\cdot \mathrm{d}\boldsymbol{l} = -K_s[\Psi + \rho g x \sin\alpha]_{x=0}^{l_c}. \tag{2.2}$$

Imposing the boundary conditions $\Psi(0) = 0$, $\Psi(l_c) = -\Psi^*$, we obtain

$$l_c \frac{\mathrm{d}l_c}{\mathrm{d}t} = K_s\Psi^* - l_c K_s \rho g \sin\alpha, \tag{2.3}$$

for a straight capillary tube.

Washburn's equation (2.3) has been widely applied to describe liquid transport in textiles (Hodgson & Berg 1987; Miller & Jansen 1982; Hollies *et al.* 1957). For horizontal capillary tubes, the flow is driven by capillary forces at the meniscus and the length of the wetted region grows diffusively according to

$$l_c = (2K_s\Psi^* t)^{1/2}. \tag{2.4}$$

When the capillary tubes are inclined downwards ($\alpha < 0$), a balance between gravitational acceleration and a retarding viscous drag force is ultimately established, with the length increasing linearly with time, according to

$$l_c = -K_s \rho g t \sin\alpha, \tag{2.5}$$

independent of the capillary pressure. When infiltration occurs in a strip of material inclined upwards ($\alpha > 0$), the encroachment distance ultimately tends to

$$l_c \to \frac{\Psi^*}{\rho g \sin\alpha}, \tag{2.6}$$

where a balance is established between capillary and gravitational forces. The difficulty in relating Washburn's model to a material having a void space of complex geometry is that the flow behind the front is assumed to be saturated and the model is restricted to unidirectional flow.

2.2. *Richards' model*

Richards developed a continuum description of transport in porous materials which now serves as the foundation for most models of infiltration. Drawing an analogy with Darcy's law for saturated flow, Richards proposed that the filtration velocity is proportional to the gradient of pressure and dependent on the moisture content. For the case of a thin sheet of porous or fibrous material where $\hat{\boldsymbol{x}}$ and $\hat{\boldsymbol{y}}$ are unit vectors oriented parallel to the sheet in the down- and cross-slope directions respectively, the filtration velocity is

$$\boldsymbol{u} = -K(\theta)(\nabla\Psi(\theta) + \rho g \sin\alpha\hat{\boldsymbol{x}}), \tag{2.7}$$

where K is the permeability, which depends on the type and interconnection between pores in the medium and on the liquid's viscosity. Both permeability and capillary pressure are functions of θ, the local moisture content. Coupling (2.7) with the conservation of mass,

$$\frac{\partial\theta}{\partial t} = -\nabla\cdot\boldsymbol{u}, \tag{2.8}$$

yields a nonlinear advection diffusion equation,

$$\frac{\partial\theta}{\partial t} = \frac{\partial}{\partial x}\left(K(\theta)\frac{\partial\Psi}{\partial x}\right) + \frac{\partial}{\partial y}\left(K(\theta)\frac{\partial\Psi}{\partial y}\right) + \rho g \sin\alpha\frac{\partial K(\theta)}{\partial x}, \tag{2.9}$$

describing flow in a thin inclined porous sheet. Equation (2.9) is commonly referred to as Richards' equation in the mixed Ψ–θ form. A large number of studies have focused on vertical infiltration (where $\alpha = \pm\pi/2$), for example in examining downward infiltration into soils, but (2.9) has not been studied for point sources on inclined fibrous sheets.

There are a number of difficulties encountered when applying Richards' equation to describe transport in porous materials. The variation of capillary pressure with moisture exhibits hysteresis as the driving pressure is first increased and then decreased (see § 3), with a fraction of the void space remaining filled with liquid after draining is complete. This translates to the pressure–moisture (Ψ–θ) relation being multivalued and precludes the application of (2.9) to a general description of infiltration, unless it is modified or additional phenomenological relations are considered. In this paper we restrict our analysis to flows where $\partial\theta/\partial t \geqslant 0$, and the Ψ–θ relationship is analytic. Nevertheless in many absorbent applications, especially those where the material's geometry leads to localized draining and imbibition, hysteresis will be important in determining the functional absorbency of a product.

Exact analytical and approximate solutions of Richards' equation have been obtained in a number of cases where the diffusivity–moisture content relation is known and single-valued (e.g. Phillip 1955; Parlange 1971). In general the highly nonlinear nature of the defining liquid-medium transport properties means that many

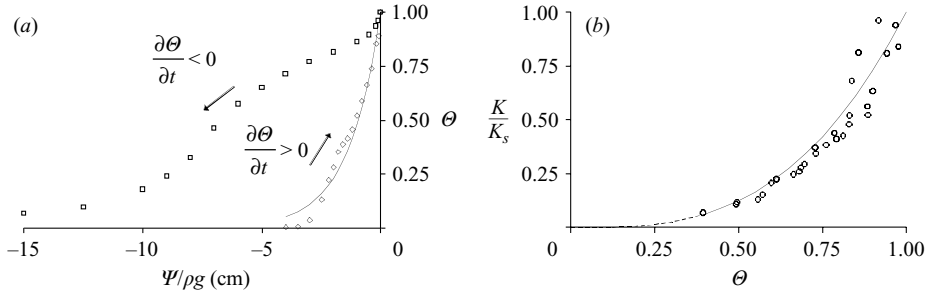

FIGURE 2. (*a*) Experimental results showing the variation of capillary pressure (Ψ) with saturation ($\Theta = \theta/\theta_s$) measured in the sample fabric. Measurements were made for liquid absorption ($\partial\Theta/\partial t > 0$), and desorption ($\partial\Theta/\partial t < 0$) from an initially dry and saturated material respectively. A pronounced hysteresis is clearly observed. (*b*) The variation of the relative permeability (K/K_s) with moisture content is shown. The dashed curve shows the region in which the moisture level was inhomogeneous.

infiltration problems can only be solved numerically. Numerical solutions to the pressure-based form of the Richards equation have been shown to suffer from poor mass conservation (Celia, Bouloutas & Zarba 1990) and there is an extensive literature dealing with this problem. An explicit numerical scheme is challenging to develop, unless saturated and unsaturated regions are separately solved and matched, because the material becomes saturated and $\mathrm{d}\theta/\mathrm{d}\Psi \to 0$.

3. Characterization of a fibrous sheet and experimental set-up

The fibrous material chosen for this study is a non-woven needlefelt fabric consisting of circular cross-sectional polyester fibres of radius 11 μm. This material was used because it has negligible swelling in water, is composed of a single fibre type and is typical of the absorbents used in reusable incontinence products. The fabric was ~ 0.55 cm thick with a void fraction, corresponding to the saturated moisture content θ_s, of 93%. Experiments were carried out in a controlled environmental chamber at 20°C and 50% relative humidity. A variety of material-specific empirical closure relations, between K, Ψ and θ, have been proposed for soils, many of which are built around assumptions about pore size distribution and lengths (for example Mualem 1976). Since the geometrical structure of fibrous materials is completely different from soils and granular media, these closure relations must be experimentally determined for the chosen fabric.

The capillary pressure–moisture (Ψ–θ) relationship was measured using a Textiles Research Institute autoporosimeter (Miller & Tyomkin 1994). For each applied pressure the equilibrium moisture content was measured – and the time taken for the moisture level to reach an equilibrium increased significantly at low capillary pressures. Moisture content was measured in the case of both liquid entering and draining from the sample (figure 2*a*) – this illustrates the pronounced hysteresis between infiltrating and draining flows.

To find the relationship between permeability and moisture content, liquid was introduced at a constant flow rate into a sample inclined vertically downwards ($\alpha < 0$). For high flow rates, the liquid was delivered using a computer-controlled pump, while for low flow rates, a gravity-driven feed was employed. The high permeability and low capillary pressure of the fabric samples means that, for constant-flux source flows down an inclined strip of material, the length of the capillary fringe is small compared

to the total wetted length in the sample. The permeability of the sample was estimated from the speed of infiltration in a gravity-driven flow. Combining the conservation of mass with Darcy's equation for steady flow from a constant flux line source yields

$$-K(\theta)\rho g \sin\alpha = \theta \frac{\mathrm{d}l_c}{\mathrm{d}t}, \tag{3.1}$$

which is in agreement with Washburn's analysis (2.5) when $\theta = 1$. Using a range of flow rates to introduce liquid into the sample the permeability–moisture relationship was determined from the translation speed of the wetting front. The moisture level is uniform along the wetted length, except in the region close to the capillary fringe, and θ can be directly determined. A similar method has been previously used to determine the permeability in soils (Youngs 1964). The permeability became difficult to determine at high flow rates where liquid pooled or ran over the fabric surface, while at low flow rates (and low values of θ), the front of the invading liquid becomes irregular, leaving dry patches as the front advances along the fabric. To avoid problems at high flow rates the saturated permeability, and hence flow rate, was measured by introducing liquid using a saturated source at zero pressure head. Figure 2(*b*) shows the variation of the relative permeability with moisture content. The dashed curve corresponds to the trend of the experimental results when the wetted region is inhomogeneous. Other approaches have been developed (e.g. Childs & Collis-George 1950) to measure the moisture diffusivity, defined for the porous material by $D = K\,\mathrm{d}\Psi/\mathrm{d}\theta$, exploiting an analogy with diffusion, but this approach is only useful when gravitational acceleration is not important.

Analytical functions need to be fitted to figure 2(a, b) in order that they may be incorporated into Richards' equation. Both the relatively good agreement with measurements and a requirement that Richards' equation is accessible to analytical study, suggest we fit

$$K(\Theta) = K_s\Theta^3, \qquad \Theta = \exp(\Psi/\Psi_*), \tag{3.2a, b}$$

to figure 2(a, b), where $\Theta = \theta/\theta_s$. The fit used for permeability is in good agreement with the experimental results (with a correlation mean square of 0.89). Power-law fits to permeability, such as (3.2a) have also been applied to soils and sands (e.g. Brooks & Corey 1966), where an exponent of 3 is typical. An exponential relationship between saturation and capillary pressure has been previously applied to describe the hydraulic properties of soils (e.g. Gardner 1958; Russo 1988). A least-squares fit to the experimental results gives $\Psi^*/\rho g = 1.36(\pm 0.16)\,\mathrm{cm}$ and $\rho g K_s = 1.00(\pm 0.14)\,\mathrm{cm\,s^{-1}}$. The large errors are attributed to the inherent variability in the properties of the material. Note that the value of $\Psi^*/\rho g$ is comparable to the sheet thickness (0.55 cm). A common feature of many permeability relations (such as Haverkamp *et al.* 1977) is the presence of a percolation threshold (typically around $\Theta_c \sim 0.4$) below which the permeability rapidly becomes small. This has the tendency to sharpen the moisture profile near the front, though this is not captured by (3.2a).

The methodology applied to characterise the material is the same as that employed to study infiltration into the fibrous sheets. In these experiments, a small quantity of dye was added to enable the wetted region to be visualized. The influence of dye on the surface tension and contact angle at the water–air–fibre interface and the infiltration properties was determined to be negligible. The fibrous sheet was placed on a flat rigid board, over which a calibrated grid was laid. Experiments were recorded and the images processed to extract measurements of the wetted region. The distribution of moisture content within samples was measured using a direct gravimetric method,

where sections of the fabric were cut and weighed, and compared to the mass of the same dry sample. Other methods, such as X-ray attenuation, may also be applied to find the moisture distribution within absorbent materials and give equivalent results (e.g. Landeryou, Yerworth & Cottenden 2003).

4. Line sources

Wicking from saturated regions (with a zero pressure head) and constant-flux source-driven flows are considered as they form the basis of the phases involved in the absorption of liquid by an absorbent incontinence product. We first describe capillary-driven flows, from saturated sources, followed by constant-flux-driven flows. By combining (3.2) and (2.9), we obtain

$$\frac{\partial \Theta}{\partial t} = \frac{\partial}{\partial x}\left(\frac{K_s \Psi^*}{\theta_s}\Theta^2 \frac{\partial \Theta}{\partial x}\right) + \frac{\partial}{\partial x}\left(\frac{K_s \rho g \sin\alpha}{\theta_s}\Theta^3\right). \tag{4.1}$$

We describe similarity and numerical solutions to (4.1) which are confirmed experimentally.

4.1. *Capillary-driven flow*

When the sample is held horizontally ($\alpha = 0$) and saturated at the origin infiltration is driven by capillary forces at the wetting front. The material is saturated only at a single point, so that the characteristic scale for the moisture content is unchanged. By applying Boltzmann's transformation $\tilde{x} = x/X(t)$ (Gardner 1958; Boltzmann 1894; Ruoff *et al.* 1959) where $X(t) = (2K_s\Psi^* t/\theta_s)^{1/2}$ and $\tilde{\Theta}(\tilde{x}) = \Theta(x, t)$ (4.1) reduces to

$$-\tilde{x}\frac{\mathrm{d}\tilde{\Theta}}{\mathrm{d}\tilde{x}} = \frac{\mathrm{d}}{\mathrm{d}\tilde{x}}\left(\tilde{\Theta}^2 \frac{\mathrm{d}\tilde{\Theta}}{\mathrm{d}\tilde{x}}\right), \qquad \tilde{\Theta}(0) = 1. \tag{4.2}$$

To find the unique solution an iterative method is used to determine when the volume flux at the origin is consistent with the global volume constraint. Other iterative methods to search for the solution have been described (e.g. Phillip 1955; Kirkham & Powers 1972). The numerical calculations show that the length of the wetted region $l_c = \lambda_{C1} X$, where $\lambda_{C1} = 0.770$. Since $\lambda_{C1} < 1$, the rate of encroachment is slower than (2.3) because the permeability is reduced for partially saturated flows. The dimensional grouping

$$A = \frac{l_c}{t^{1/2}}, \tag{4.3}$$

is applied to interpret the experimental measurements. Figure 3(*a*) shows experimental measurements of the saturation profile during infiltration from a reservoir, where one end of the sample is saturated but with no pressure head. X-ray images show that infiltration is characterized by a markedly inhomogeneous moisture distribution, on a scale comparable to the size of the needles used during manufacturing to consolidate the material.† Liquid invasion appears to first advance the wetting interface through higher capillary pressure regions, with subsequent back filling behind the wetting front. Figure 3(*b*) shows the moisture profile during horizontal infiltration at different times, normalized using the length of the wetted region. The experimental measurements confirm that the moisture profile tends to a similarity form. A comparison with the

† These nonwoven fabrics are produced from a fibrous assemblage that is consolidated by being passed through a bed of oscillating barbed needles.

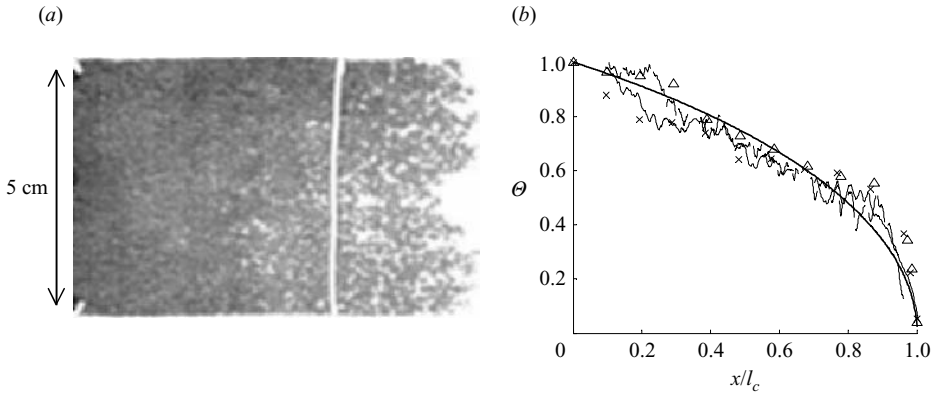

FIGURE 3. (*a*) The X-ray image (40 keV, 100 mA, 0.6 s) shows the moisture distribution during horizontal wicking from a large reservoir – the dark regions show wet fabric. The vertical white band is a metal marker used as a reference scale which has been masked out. (*b*) Moisture variation along a fabric section during horizontal wicking, when the front has infiltrated a distance l_c. Thin solid and dashed lines show averaged moisture distribution measurements from wetted sections, using X-ray attenuation for $l_c = 8$ and 16 cm respectively. The symbols show gravimetric measurements of moisture content for $l_c = 50$ (×) and 75 cm (△). The moisture profile calculated using the similarity solution is plotted as a bold line.

similarity solution shows a major difference near the front of the wetted region, where the profile is sharper than predicted. This was attributed to a percolation threshold (see comments in § 3) which is not included in (4.1). By combining experimentally determined values of K_s and Ψ^* (from § 3) with (4.3) we estimate $A_T = 1.32\,\mathrm{cm\,s^{-1/2}}$, while experimental measurements show that $A_E = 1.1\,\mathrm{cm\,s^{-1/2}}$. The effect of a percolation threshold is to slightly reduce A_T, bringing it closer to the experimental value A_E.

When the sample is inclined below the horizontal ($\alpha < 0$), and a balance between viscous and buoyancy forces is ultimately achieved, the length of the wetted region increases at a constant rate

$$l_c = -\frac{K(\theta)\rho g t \sin\alpha}{\theta}. \tag{4.4}$$

When the sheet is inclined above the horizontal, ($\alpha > 0$), the moisture profile eventually reaches a steady state with a balance between gravity and capillary forces yielding

$$\Theta(x) = \exp\left(-\frac{x\sin\alpha}{\Psi^*/\rho g}\right). \tag{4.5}$$

Figure 4 shows a comparison between (4.5) and experimental measurements of the saturation profiles measured vertically for capillary-driven flows at a number of angles of inclination. To prevent liquid redistribution during sectioning of the samples, the sample was frozen once it had reached steady state, and a gravimetric method applied. In this configuration, the local pressure decreases hydrostatically as $\Psi/\rho g = -x\sin\alpha$ and is equivalent to the measurements described in figure 2(*a*). For very low angles of inclination the variation of moisture across the fabric thickness became increasingly important.

4.2. *Source-driven flow*

When fluid is introduced at a constant areal flux q_a (where the areal flux includes the effect of porosity) along a line source, (4.1) is solved in conjunction with a global

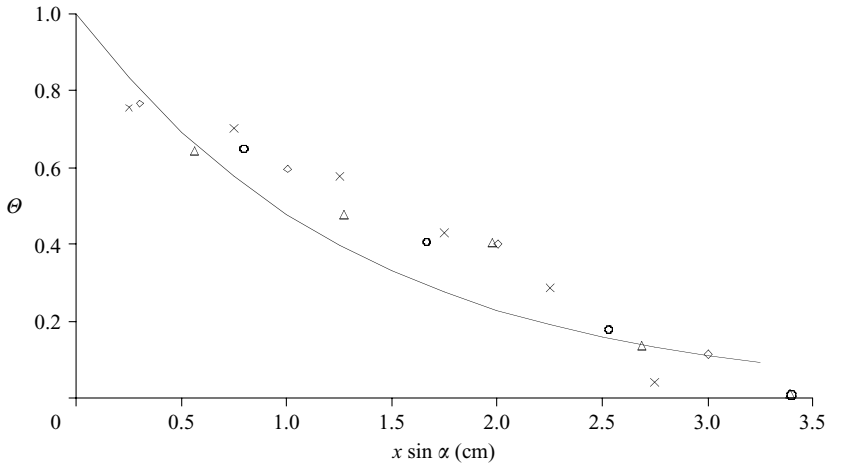

FIGURE 4. Equilibrium moisture profile between wicking and gravity for a sample inclined at an angle α above the horizontal from a large reservoir ($\times$, $\alpha = 30°$; $\triangle$, 45°; $\bigcirc$, 60°; $\diamond$, 90°). Equation (4.5) is plotted as a full line.

volume constraint:

$$\int_0^{l_c} \Theta \, \mathrm{d}x = q_a t, \tag{4.6}$$

where l_c is the length of the wetted region.

We first consider the case of a horizontal sheet ($\alpha = 0$). Physically, the moisture level close to the source rapidly increases until it becomes saturated, after which the saturated front and capillary fringe are advected with a constant speed along the sheet. The initial saturation of the fibrous sheet, for $\Theta(0, t) < 1$, can be calculated from a similarity solution of the form $\Theta = \Gamma(t)\tilde{\Theta}(\tilde{x})$, where $\Gamma(t) = (9q_a^2\theta_s/4K_s\Psi^*)^{1/4}t^{1/4}$, $X(t) = (4q_a^2K_s\Psi^*/9\theta_s)^{1/4}t^{3/4}$, and $\tilde{x} = x/X(t)$, which reduces Richards' equation (4.1) to

$$\frac{\mathrm{d}^2\tilde{\Theta}^3}{\mathrm{d}\tilde{x}^2} = \frac{1}{3}\tilde{\Theta} - \frac{\tilde{x}}{3\tilde{\Theta}^2}\frac{\mathrm{d}\tilde{\Theta}^3}{\mathrm{d}\tilde{x}}, \qquad \int_0^{\lambda_{S1}} \tilde{\Theta}(\tilde{x}) \, \mathrm{d}\tilde{x} = 1. \tag{4.7a, b}$$

The numerical solution which satisfies (4.7*a*) and the constraint (4.7*b*), corresponds to $\lambda_{S1} = 1.36$ and $\tilde{\Theta}(0) = 1.09$. The similarity solution breaks down when the flow is saturated, which first occurs at the origin when $\Theta(0, t) = \Gamma(t)\tilde{\Theta}(0) = 1$. Figure 5(*a*) shows experimental measurements of the wetted length, compared to the similarity solution for a number of low flow rates, and good agreement is observed, up to time $t/(A/q_a)^2 = 0.26$, after which the similarity solution (4.7*a*, *b*) is rendered invalid because $\Theta = 1$. In normalizing the experimental and theoretical results we use A_E and A_T respectively. The experimental results are reproducible in this region, but consistently lie beneath the similarity solution. This was attributed to a false time and position origin caused by introducing the source at a finite, but small (~ 0.5 cm) distance from the end of the fabric. After a long time ($t/(A/q_a)^2 \gg 0.26$) the moisture profile is advected with speed q_a and consists of a capillary fringe at the front of the flow, behind which the material is saturated. Transforming (4.1) to the steady frame advancing with the front of the fringe (l_c) using $x' = x - l_c$, yields

$$q_a \frac{\mathrm{d}\Theta}{\mathrm{d}x'} = \frac{K_s\Psi^*}{\theta_s}\frac{\mathrm{d}}{\mathrm{d}x'}\left(\Theta^2\frac{\mathrm{d}\Theta}{\mathrm{d}x'}\right), \tag{4.8}$$

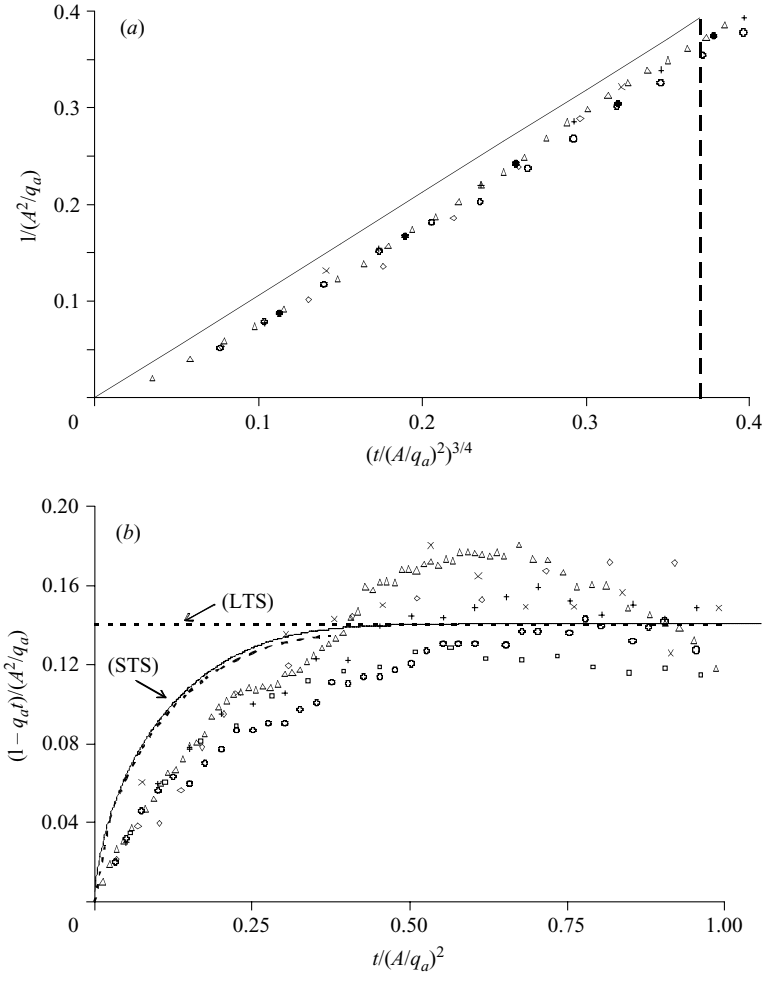

FIGURE 5. (*a*) Experimental measurements of the wetted length with time for a constant volumetric flux ($q_a = \triangle$, 0.02; $\bullet$, 0.04; $\circ$, 0.05; $\diamond$, 0.07; $+$, 0.08; $\times$, 0.1 cm s^{-1}), applied to the end of a 2 cm wide strip of fabric. The short-time similarity solution is plotted as a full line up to the time $(t/(A/q_a^2))^{3/4} = 0.36$. (*b*) Development of the wetted length during infiltration into a horizontal fabric sample, plotted as $(l_c - q_a t)$ versus time. The short- (STS) and long- (LTS) time similarity solutions are plotted as dashed lines, while the numerical solution is plotted as a full line.

whose solution is $\Theta = (-2q_a x'\theta_s/K_s\Psi^*)^{1/2}$ for $x' > -K_s\Psi^*/2q_a\theta_s$. The front moves with a speed q_a because the fabric is saturated behind the capillary fringe. A measure of the length of the capillary fringe is $l_c - q_a t$, which for large time tends to

$$l_c - q_a t = \frac{K_s\Psi^*}{6q_a\theta_s} = \frac{A^2}{12q_a\lambda_{C1}^2}. \tag{4.9}$$

Figure 5(*b*) shows the variation of the length of the capillary fringe with time t, along with a comparison between numerics, short- and long-time similarity solutions, and experimental results. As infiltration progresses the sample eventually becomes saturated close to the point of introduction. The scatter in figure 5(*b*) is due to errors in measuring the wetted length arising because the front is irregular and the capillary

fringe is small relative to the saturated length. The ultimate length of the capillary fringe expected from (4.9) is also shown in figure 5(*b*), and agrees with the experimental measurements, over a decade range in q_a. Experimental measurements confirm the initial increase in $l_c - q_a t$. In the experiment liquid is not confined to the sample, which is unable to sustain a positive pressure when saturated, and as a result liquid tends to leak leading to a decrease in $l_c - q_a t$ after some time, a process not captured by the model. The time and position offsets seen in figure 5(*b*) are the same as in figure 5(*a*), which tends to explain the difference between the experimental results and similarity solution.

When the fibrous sheet is tilted below the horizontal ($\alpha < 0$), the moisture profile is uniform along the length of the wetted region except close to the capillary fringe. Over the uniformly wetted region the length l_c is related via the mass conservation to the rate of liquid introduction (from (4.6)), through

$$\Theta l_c = q_a t. \tag{4.10}$$

By combining (3.1) and (4.10), the permeability is estimated to be

$$K(\Theta) = -\frac{q_a \theta_s}{\rho g \sin\alpha}. \tag{4.11}$$

As described in § 3 (see (3.1)), this is essentially how the permeability is measured experimentally. For $K(\Theta) = K_s \Theta^3$ (combining (4.11) and (4.10)) the encroachment distance is

$$l_c = q_a^{2/3} \left(\frac{-K_s \rho g \sin\alpha}{\theta_s} \right)^{1/3} t. \tag{4.12}$$

For upslope flow ($\alpha > 0$), a saturated liquid body is driven upwards by the source. The similarity moisture profiles at the front of the capillary fringe for vertical upward and downward infiltration have recently been studied by Witelski (2003).

5. Point sources

5.1. *Spreading on a horizontal sheet* ($\alpha = 0$)

Ruoff *et al.* (1959) describe the application of Boltzmann's transformation to radial transport from a point into a sheet of paper. To calculate radial transport from a saturated point the diffusivity–moisture relation was applied, this relation being obtained using the moisture profile from a line source. We extend these calculations to examine radial flow driven by a source.

The sheet is initially dry ($\Theta(x, y) = 0$, at $t = 0$), and fluid is introduced at the origin. Both source- and capillary-driven flows on a horizontal sheet generate a circular wetted region whose radius grows with the square root of time and so they can be treated within the same framework (with different boundary conditions). Rescaling the radial distance as $\tilde{r} = r/R(t)$ where $R = (2K_s \Psi^* t/\theta_s)^{1/2}$ reduces Richards' equation (4.1) to

$$\frac{\mathrm{d}^2 \tilde{\Theta}^3}{\mathrm{d}\tilde{r}^2} = \left(-\frac{\tilde{r}}{\tilde{\Theta}^2} - \frac{1}{\tilde{r}} \right) \frac{\mathrm{d}\tilde{\Theta}^3}{\mathrm{d}\tilde{r}}, \qquad \int_0^{\lambda_{S2}} \tilde{\Theta} \tilde{r}\, \mathrm{d}\tilde{r} = \gamma, \qquad \tilde{r} \tilde{\Theta}^2 \frac{\mathrm{d}\tilde{\Theta}}{\mathrm{d}\tilde{r}} \bigg|_{\tilde{r} = \tilde{r}_s} = -\frac{\gamma}{2}, \quad (5.1a, b, c)$$

where

$$\gamma = \frac{Q_a \theta_s}{4\pi K_s \Psi^*} \tag{5.2}$$

expresses the rate of increase of the wetted region due to a driving source compared to pure infiltration. The radius of the wetted region is $r_c = \lambda_{S2} R$. The distance $\tilde{r}_s$ (see (5.1*c*)), which is determined as part of the solution, corresponds to the point at which the moisture level initially decreases.

For $\gamma \gg 1$, the flow is characterized by a saturated core and a thin capillary fringe so that $\lambda_{S2} \to (2\gamma)^{1/2}$ since $r_c^2 = Q_a t/\pi$. Near the front of the wetted region, the moisture level Θ diminishes to zero. The local singularity in the gradient of the moisture at $\tilde{r} = \lambda_{S2}$ can be estimated from (5.1*a*) to be

$$\Theta \sim (2\lambda_{S2})^{1/2}(\lambda_{S2} - \tilde{r})^{1/2}. \tag{5.3}$$

This expression for $\gamma \ll 1$ provides a leading-order description of the moisture profile everywhere except near the origin. But as the volume of fluid in the near-source region is small we can apply (5.1*b*) to determine the relationship between λ_{S2} and γ, which is

$$\lambda_{S2} \sim \frac{15^{1/3}\gamma^{1/3}}{2^{5/6}}. \tag{5.4}$$

For capillary-driven flows, an additional constraint that the fabric is saturated at the origin ($\Theta = 1$ at $\tilde{r} = 0$) is applied. Since the flux is determined as part of the solution, the size of the source has an effect on the infiltration rate. By systematically reducing the source size we estimate $\gamma_c = 0.028$, $\lambda_{C2} = r_c/R = 0.40$ for capillary-driven infiltration.

Figure 6(*a*) shows experimental measurements of the variation of r_c^2 with time, confirming that $r_c \sim t^{1/2}$. For high flow rates, the fraction of the wetted region which forms the capillary fringe decreases – at the highest flow rates, liquid tends to pool near the source and the measured radius falls under the solid curve, $r_c^2 = Q_a t/\pi$, which corresponds to complete saturation. Figure 6(*b*) shows the variation of $\lambda_{S2} = r_c/R$ with γ. Good agreement is observed between the experimental measurements and the similarity solution. Figure 6(*b*) also shows the transition between a saturated and unsaturated core, which corresponds to wicking from a reservoir at zero pressure head, which is indicated by $\gamma = \gamma_c$.

Experimental measurements for wicking from a saturated point confirm the Boltzmann scaling for r_c, and a ratio between planar and point-source infiltration of ~ 1.54, compared with a theoretical value of $\lambda_{C1}/\lambda_{C2} = 1.93$. These results also show that the encroachment distance for infiltration from a saturated planar source is greater than from a point source. Washburn's analysis indicates that both should proceed at the same rate.

The moisture profile changes substantially with γ. As indicated in figure 7, the size of the capillary fringe decreases as γ increases. Agreement is observed between the similarity solution and experimental measurements of the saturation for two contrasting flow rates. Note, the measured moisture level in these experiments is lower than 0.4 close to the front of the wetted region as a result of sectioned samples including significant unwetted portions near the irregular front.

5.2. *Spreading on an inclined sheet* ($\alpha < 0$) *from a point source*

Non-dimensionalizing (2.9) using

$$L = -\Psi^*/\rho g \sin\alpha, \quad T = \theta_s \Psi^*/K_s \rho^2 g^2 \sin^2\alpha, \quad \hat{x} = x/L, \quad \hat{y} = y/L, \quad \hat{t} = t/T, \tag{5.5}$$

gives

$$\frac{\partial \Theta}{\partial \hat{t}} + \frac{\partial \Theta^3}{\partial \hat{x}} = \frac{\partial}{\partial \hat{x}}\left(\Theta^2 \frac{\partial \Theta}{\partial \hat{x}}\right) + \frac{\partial}{\partial \hat{y}}\left(\Theta^2 \frac{\partial \Theta}{\partial \hat{y}}\right). \tag{5.6}$$

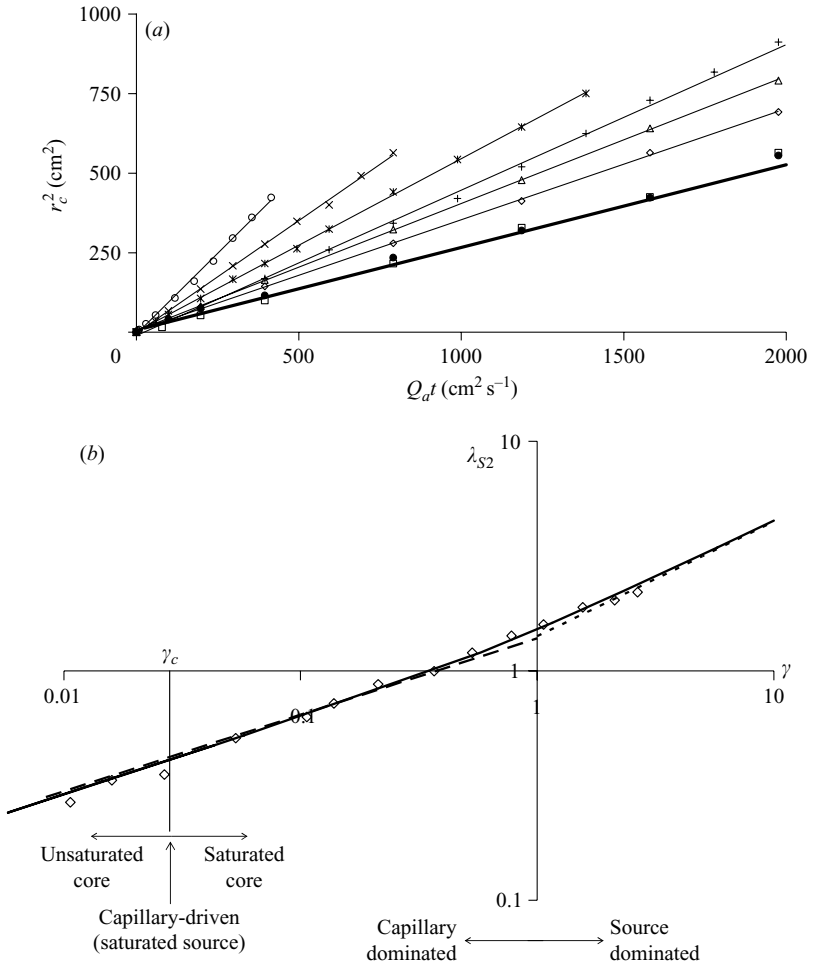

FIGURE 6. (*a*) Radius of the wetted region during horizontal infiltration from a point source ($Q_a = \circ$, 0.3; $\times$, 1; $*$, 2; $+$, 4; $\triangle$, 9.8; $\diamond$, 19.6; $\square$, 39.1; $\bullet$ 48.9 cm^2 s^{-1}). The thick solid line represents the growth of the wetted radius for a saturated material. (*b*) Experimental measurements of $\lambda_{S2} = r_c/R$ versus γ, the relative strength of source-driven to capillary-driven flow. Capillary-driven flow from a saturated point corresponds to $\gamma = \gamma_c$. The dashed line is the estimate (5.4), and the dotted line is $\lambda_{S2} = (2\gamma)^{1/2}$; the full curve is obtained from the similarity solution.

According to (4.5), L is the characteristic distance fluid will infiltrate upstream of the source ($x < 0$). Equation (5.6) is solved subject to the volume constraint

$$\int_{-\hat{X}_T}^{\hat{X}_N} \int_{-\hat{Y}_W}^{\hat{Y}_W} \Theta \, \mathrm{d}\hat{y} \, \mathrm{d}\hat{x} = 4\pi\gamma\hat{t}, \tag{5.7}$$

where γ is defined by (5.2) and is independent of the sheet angle. The length L characterises the infiltration distance upslope of the source (see (4.5)). The maximum half-width of the wetted region and downslope length (from the source) are denoted by $\hat{Y}_W$ and $\hat{X}_N$ respectively; the upstream wetted distance is $\hat{X}_T$.

When $\hat{X}_N \ll 1$, corresponding to short time $\hat{t} \ll 1$, the influence of downslope gravitational acceleration is weak, and (5.6) and (5.7) reduce to (5.1). In this case

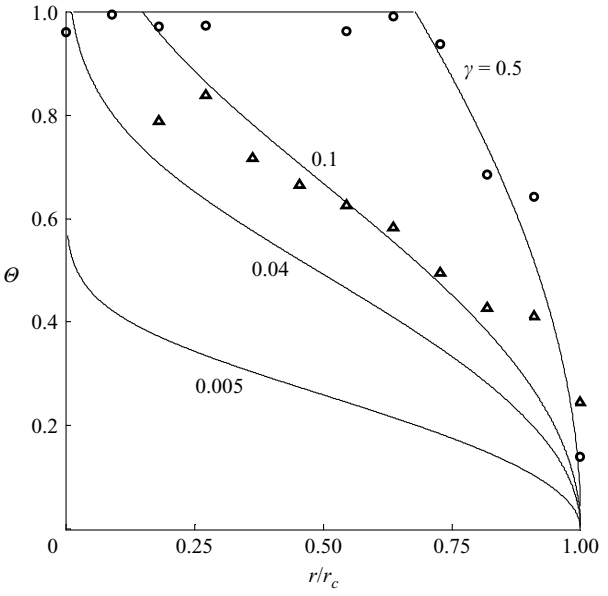

FIGURE 7. Similarity radial moisture profiles generated by source-driven flows are plotted for four values of γ. Experimental measurements of the moisture profiles for $\gamma = 0.1$, 0.5 are plotted as $\triangle$ and $\circ$ respectively. The moisture content was determined gravimetrically using samples from a 10° triangular wedge of material.

the transport processes are understood from § 5.1, which recast in dimensionless form yields $\hat{X}_N = \hat{Y}_W \sim \lambda_{S2}\sqrt{2\hat{t}}$. As $\hat{t}$ increases, we anticipate and later confirm that downslope gravitational acceleration becomes important and $\hat{X}_N$ grows faster than $\hat{t}^{1/2}$, while the cross-slope width $\hat{Y}_W$ ultimately grows more slowly than $\hat{t}^{1/2}$.

To explore the dynamics at intermediate and large time, we must appeal to full numerical solutions. In contrast to a line source on an inclined sheet, (5.6) and (5.7) do not admit a similarity solution for large time. By developing an approximate description of the steady near-source flow, we are then able to calculate how $\hat{X}_N$ and $\hat{Y}_W$ vary with $\hat{t}$ and γ.

5.2.1. *Numerical solutions*

Explicit and implicit time marching methods, accurate to second order in space, were applied to solve (5.6). A volume source was introduced onto the right-hand side of (5.6), located at the origin. For an explicit implementation, the computational domain was partitioned into saturated and unsaturated regions which were solved separately and matched. To cope with a wide range of $\hat{t}$ (over 6 decades), the computational domain was resized. Both the explicit and implicit implementations were tested against one another and validated against the similarity solutions described in § 5.1.

As anticipated, the size of the pool of liquid increases with γ, which denotes the ratio of source strength to wicking action. Figure 8(a, b) shows the variation of $\hat{X}_N$ and $\hat{Y}_W$ with time for $\gamma = 0.01$, 0.1, and 1. For $\hat{t} \ll 1$ the numerical results agree with the similarity solutions (denoted by the dashed line) from § 5.1.

Figure 9 shows the moisture profiles for $\gamma = 0.01$, 0.1 and 1, at three times. The shaded region shows where the rate of change in the moisture level is smaller than $\partial\Theta/\partial t < 2.5 \times 10^{-4}$. The region where $\partial\Theta/\partial t$ is small, occupies a finite fraction of the wetted region and appears to grow in proportion to its dimensions. For large time,

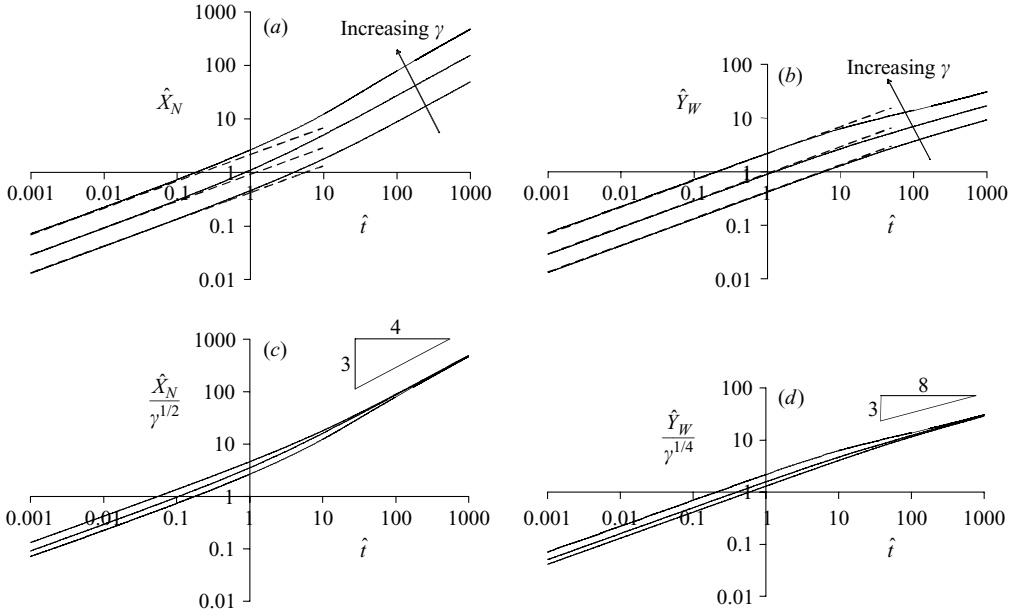

FIGURE 8. Numerical results describing the increase in (*a*) the downslope length, $\hat{X}_N$, and (*b*) the cross-slope half width, $\hat{Y}_W$, of the wetted region as a function of dimensionless time $\hat{t}$, for $\gamma = 0.01$, 0.1, 1. The dashed curves show the similarity solution $\hat{Y}_W = \hat{X}_N = \lambda_{S2}\sqrt{2\hat{t}}$ valid for $\hat{t} \ll 1$. The downslope length and cross-slope width are normalised using $\gamma^{1/2}$ in (*c*) and $\gamma^{1/4}$ in (*d*), respectively.

the near-source region tends to a steady form. To interpret the growth of the wetted region, we focus on the steady near-field component and develop an approximate description of the moisture profile in this region. Figure 10 appears to show that the shape of the wetted region tends to self-similar form.

5.2.2. *Steady near-source moisture profile*

For large time, the near-source flow ultimately tends to a steady state described by

$$\frac{\partial \Theta^3}{\partial \hat{x}} = \frac{1}{3}\left(\frac{\partial^2}{\partial \hat{x}^2} + \frac{\partial^2}{\partial \hat{y}^2}\right)\Theta^3, \tag{5.8}$$

in those regions where the flow is not saturated, i.e. $\Theta < 1$. The volume flux constraint enters into the solution through the mass flux condition downstream of the source,

$$\int_{-\infty}^{\infty} \Theta^3 \mathrm{d}\hat{y} = 4\pi\gamma. \tag{5.9}$$

The steady state is therefore described in the partially saturated region by a linear advection–diffusion equation in Θ^3.

A solution to (5.8) which satisfies (5.9), but for which Θ may be locally larger than unity near the source, is

$$\Theta(\hat{x}, \hat{y}) = (6\gamma)^{1/3} \exp\left(\tfrac{1}{2}\hat{x}\right)\left[K_0\left(\tfrac{3}{2}(\hat{x}^2 + \hat{y}^2)^{1/2}\right)\right]^{1/3} \tag{5.10}$$

(Bretherton 1961) where K_0 is a modified Bessel function of the second kind (Abramowitz & Stegun 1964). The agreement between (5.10) and the full numerical

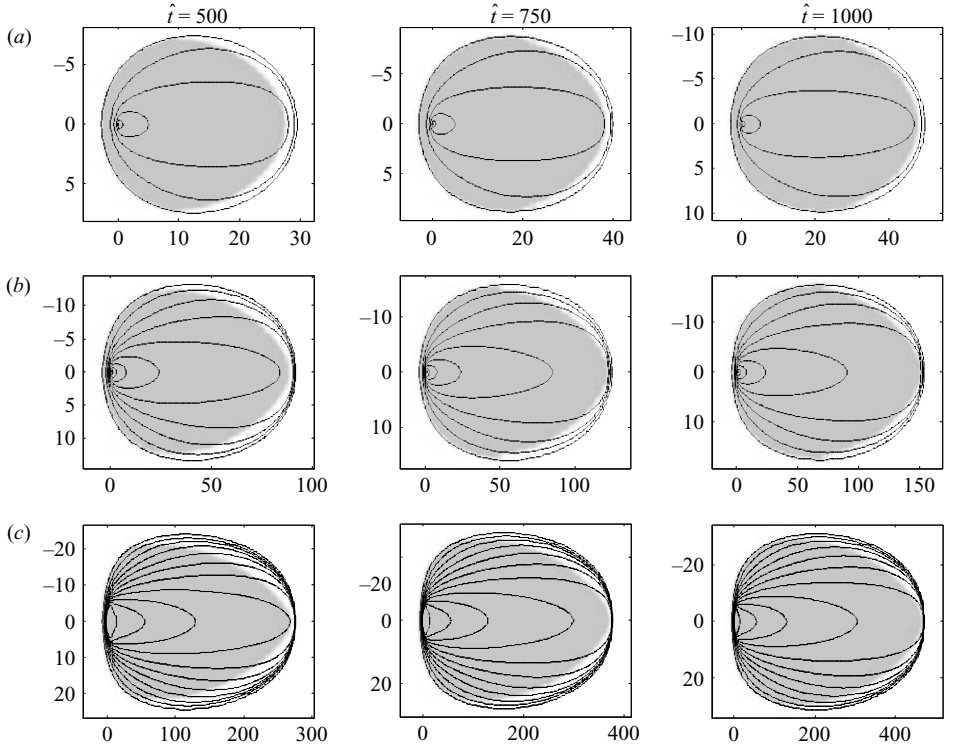

FIGURE 9. Contours of moisture saturation for (*a*) $\gamma = 0.01$, (*b*) 0.1 and (*c*) 1 for three times. The moisture contours range from 0.1 to 1 in increments of 0.1, with the wetted region shown by a contour of 0.01. The portion where the moisture content has reached steady state ($\partial\Theta/\partial t < 2.5 \times 10^{-4}$) is indicated by the shaded region.

solution is good (figure 11) for $\gamma = 0.01$ and 0.1, except very close to the source where the analytical solution fails to describe the saturation. For $\gamma = 1$, the saturated region (where $\Theta = 1$) forms a large fraction of the region plotted and the agreement with (5.10) in the near-source region is poor, but the agreement improves significantly far from the source.

Far downstream from the source, gravity-driven downslope transport dominates over capillary-driven cross-slope transport, and the moisture profiles tend to

$$\Theta(\hat{x}, \hat{y}) = (6\gamma)^{1/3} \left(\frac{\pi}{3}\right)^{1/6} \frac{1}{\hat{x}^{1/6}} \exp\left(-\frac{3\hat{y}^2}{4\hat{x}}\right), \tag{5.11}$$

since $K_0(z) \sim (\pi/2z)^{1/2} \exp(-z)$ (Abramowitz & Stegun 1964). According to (5.11), Θ decays rapidly as $\hat{y} \to \infty$. The width of the wetted region, $\hat{Y}_W$, identified with a contour of a particular value of Θ, is

$$\hat{Y}_W = \left[\frac{4}{3}\hat{x}\left(-\log\Theta + \frac{1}{6}\log\left(\frac{\hat{x}}{12\pi\gamma^2}\right)\right)\right]^{1/2}. \tag{5.12}$$

Since the moisture profile decays slowly with downslope distance, the width grows approximately as $\sim (4\hat{x}/3)^{1/2}$.

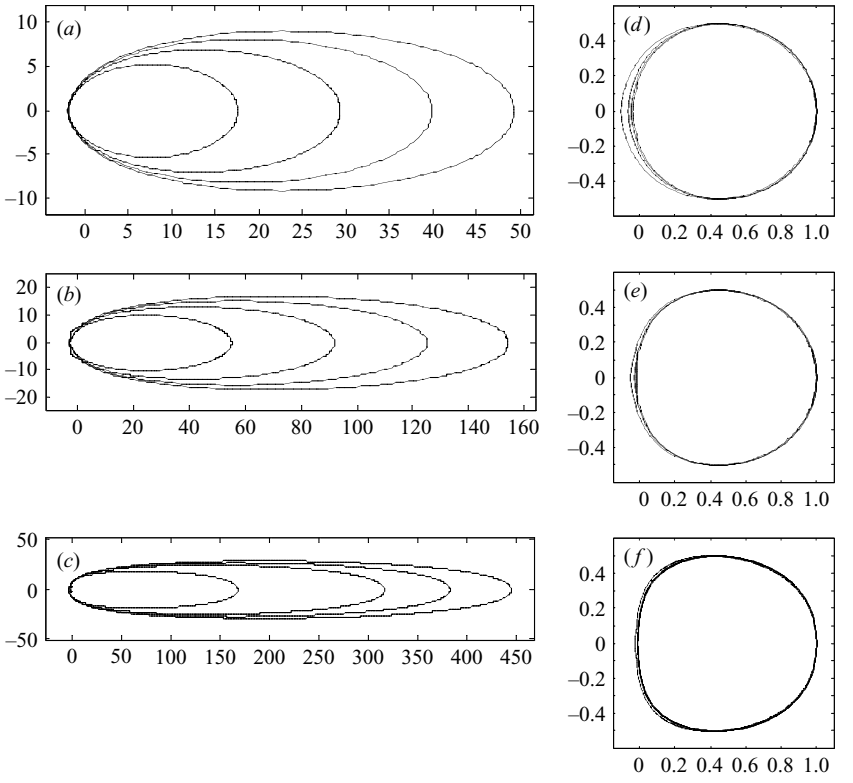

FIGURE 10. Shape of the wetted region obtained from numerical simulation of infiltration from a point source, characterized by (*a*) $\gamma = 0.01$, (*b*) 0.1, (*c*) 1 at $\hat{t} = 250$, 500, 750, and 1000. The shape of the wetted regions normalized to their cross-slope width and downslope length corresponding to (*a*), (*b*) and (*c*) are shown in (*d*), (*e*) and (*f*) respectively.

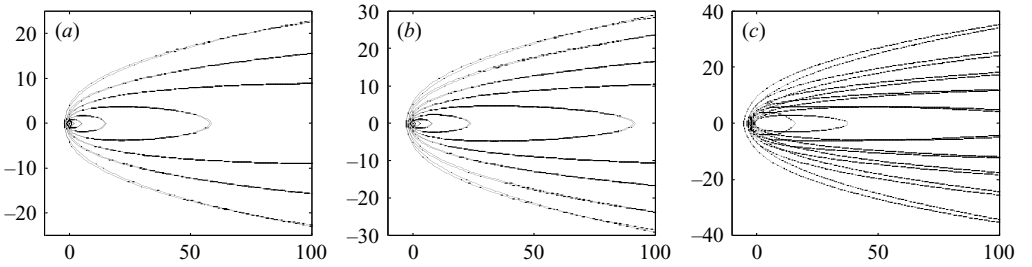

FIGURE 11. Moisture profiles for the steady near-source flow, corresponding to (*a*) $\gamma = 0.01$, (*b*) 0.1, and (*c*) 1. Full numerical solutions are plotted with a full line, while the analytical approximation (5.10) is plotted as dashed lines. The contours of saturation increase from 0 to 1 in increments of 0.05, 0.1 and 0.2 for (*a*), (*b*) and (*c*) respectively.

5.2.3. *Intermediate time scales*

At intermediate and long times, similarity methods cannot be applied for constant-flux source flows. An approximate description of the growth of the wetted region may be developed by solving (5.6) subject to $\partial\Theta/\partial\hat{t} = 0$, which enables the long-time scalings for the dimensions of the wetted region to be estimated. The volume of fluid

in this region is equal to

$$4\pi\gamma\hat{t} = \int_{-\hat{X}_T}^{\hat{X}_N} \int_{-\infty}^{\infty} \Theta(\hat{x}, \hat{y})\, \mathrm{d}\hat{y}\, \mathrm{d}\hat{x}. \tag{5.13}$$

Since the moisture level is approximately steady over a large fraction of the flow (see figure 9), we approximate $\hat{X}_T \sim 0$ and substitute (5.11) into (5.13) to obtain

$$4\pi\gamma\hat{t} \approx \int_0^{\hat{X}_N} 2(12)^{1/6}\pi^{2/3}\gamma^{1/3}\hat{x}^{1/3}\, \mathrm{d}\hat{x}. \tag{5.14}$$

Integrating (5.14), we obtain the following estimates of the dimensions of the wetted region:

$$\hat{X}_N(\hat{t}) \sim 2.0\gamma^{1/2}\hat{t}^{3/4}, \qquad \hat{Y}_W(\hat{t}) \sim \left[\tfrac{4}{3}\hat{X}_N\right]^{1/2} = 3.5\gamma^{1/4}\hat{t}^{3/8}. \tag{5.15}$$

These expressions suggest how the dimensions of the wetted region scale with $\hat{t}$ and γ. Guided by (5.15), the numerical solutions are rescaled as $\hat{X}_N/\gamma^{1/2}$ and $\hat{Y}_W/\gamma^{1/4}$ and replotted in figure 8(c, d). The numerical calculations appear to confirm the dependence of $\hat{X}_N$ and $\hat{Y}_W$ on both $\hat{t}$ and γ. Fitting the characteristic curves to figure 8(c, d), we obtain

$$\hat{X}_N \sim 2.7\gamma^{1/2}\hat{t}^{3/4}, \qquad \hat{Y}_W \sim 2.2\gamma^{1/4}\hat{t}^{3/8}. \tag{5.16}$$

The use of the steady approximation in (5.14) means that the cross-slope width is overpredicted, while the downslope length is underpredicted, as confirmed by comparing the leading coefficients of (5.15) with (5.16).

5.2.4. *Comparison with experimental results*

To test experimentally the underlying scalings (5.16) for the wetted region, a wide range of γ was required because of the insensitivity of $\hat{X}_N$ and $\hat{Y}_W$ to γ, as indicated in figure 8(a, b). Experiments were conducted at low and high flow rates ($Q_a = 0.49$ and 39.1 $\mathrm{cm^2\,s^{-1}}$) corresponding to $\gamma = 0.027$ and 2.12 (respectively), and over a wide range of α (between 1° and 50°). Fabric sheets of 1 m square in size were used, and liquid spreading recorded until it reached the bottom of the sample (having a typical downslope distance of 75 cm).

Figure 12(a, b) confirms that for $\hat{t} < 1$, where downslope gravitational acceleration is negligible, the measured wetted radii are consistent with the experiments and theory for horizontal sheets in § 5.1. For large time, a pronounced asymmetry in the later shape of the wetted region is observed, as shown in figure 12.

At longer times, the rescaled measurements of the downslope length (for high and low values of γ) collapse, though the model underpredicts the experimental measurements. As indicated in figure 8 the time taken for the collapse of $\hat{Y}_W/\gamma^{1/4}$ corresponds to approximately $\hat{t} > 100$ which is comparable to, or beyond, the timescale of the experiments. The model slightly underpredicts the downslope length, but overpredicts the cross-slope width of the wetted region. In this case the cross-slope width tends to a constant value, and as a result liquid runs faster downslope than expected. This is seen in figure 12(c) as an upturn in $\hat{X}_N$ for $\hat{t} > 100$.

For large time, the width of the wetted region tends to a constant as a consequence of a percolation threshold in moisture below which the permeability is small. While a percolation threshold has a negligible impact on flows driven in one direction (except near the nose of the wetted region), it does have a profound impact on cross-slope transport. An upper limit of the wetted width can be estimated from

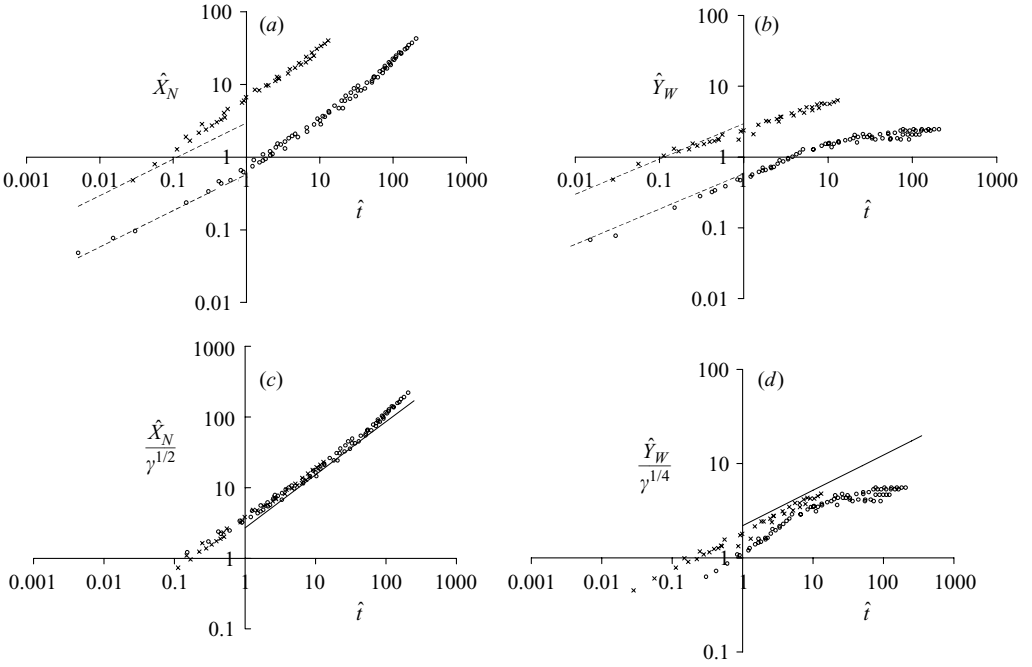

FIGURE 12. Experimentally measured cross- and downslope widths for spreading from a constant-flux source into an inclined fibrous sample. Liquid is introduced at two constant rates (○, $Q_a = 0.49$; ×, 39.1 cm^2 s^{-1} corresponding to $\gamma = 0.027$ and 2.12) and the angle of inclination varied (α varied between 1° and 50°) to obtain results over a wide range of $\hat{t}$. The downslope ($\hat{X}_N$) and half-width ($\hat{Y}_W$) of the wetted regions were measured. The short-time similarity solutions ($\hat{X}_N = \hat{Y}_W \sim \lambda_{S2}\sqrt{2\hat{t}}$) are plotted as dashed lines in (*a*) and (*b*). In (*c*) and (*d*) the down- and cross-slope dimensions of the wetted region are normalised by $\gamma^{1/2}$ and $\gamma^{1/4}$ respectively. The full lines in (*c*) and (*d*) are (5.16) which describes longer time spreading.

mass conservation, by assuming the moisture profile level drops to the percolation threshold Θ_c, $2Y_W K(\Theta_c)\rho g \sin\alpha \sim Q_a\theta_s$. In dimensionless form, the width tends to $\hat{Y}_W \sim 2\pi\gamma/\Theta_c^3$. For a typical value of $\Theta_c \sim 0.4$ the maximum current width can be estimated as $\hat{Y}_W \sim 2.65$, which compares well with $\hat{Y}_W \sim 2.46$ (for $\gamma = 0.027$). From (5.16) we estimate that the long-time analysis breaks down at $\hat{t} \sim (2\pi/\Theta_c^3)^{8/3}\gamma^2 \sim 18.3$, consistent with the measurements shown in figure 12(*b*). After this time the length grows in proportion to time and the width tends to a constant.

The heuristic modelling approach adopted in this study means that the accuracy of predictions is determined by the correctness of the closure relationships used.

5.3. *Capillary-driven flow on an inclined sheet* ($\alpha < 0$) *from a point source*

At short time ($\hat{t} \ll 1$), downslope gravitational acceleration is weak and the analysis of § 5.1 shows that the volume of fluid absorbed by the fabric increases linearly with time and $\gamma_c = Q_a\Theta_s/4\pi K_s\Psi^* = 0.028$. But at long time ($\hat{t} > 1$), gravitational acceleration is important and numerical calculations confirm that the volume of absorbed fluid increases with time, but at a slightly reduced rate. Thus while there is a significant change in the asymmetric growth of the wetted region between short and long time, the rate of absorption is only fractionally changed.

6. Concluding remarks

We have presented a study of flows through inclined fibrous sheets, which are maintained either by wicking from saturated regions or by constant-flux sources.

The new aspect of this study lies in the application of Richards' equation to describe flow in thin layers (such as fibrous sheets) using empirically determined closure relations between permeability, capillary pressure and moisture. For fibrous materials, the experimental methods – typically applied to porous media – were refined to cope with high permeabilities and low capillary pressures. The major challenge here is that the capillary wicking heights are, in many cases, only a few times the sheet thickness and the influence of a weak reservoir pressure is pronounced.

In applying Richards' continuum approach to the general problem of unsteady multiple releases into fabrics, we also need to develop closure relations which account for the hysteretic Ψ–θ relationship. The methodology described here, developing material specific closure relations, can be applied more generally to other fluid transport problems within fabrics. Recent measurements suggest that the semi-empirical forms of the closure relations developed are similar for other non-woven polyester needlefelts, and our general conclusions also apply.

The theoretical predictions were tested experimentally using intrusive (e.g. gravimetric) and non-invasive (e.g. optical and X-ray) methods, and the agreements were satisfactory. Experimental measurements support the scalings of the downslope length of the wetted region. However, for weak sources or long time, the existence of a percolation threshold in the permeability has an impact on the spread of fluid. The percolation threshold places a limit on the time up to which the analysis in § 5.2 holds. The inclusion of a percolation threshold into the model may be achieved by modifying the permeability–moisture relationship.

Practical application of the models and closure relationships to medical adsorbents is relatively straightforward, requiring representative incontinence pad geometry and discharge rate. In these applications hysteresis is likely to play a significant role (above all in geometries where α changes sign) and these additional effects must be considered. A current challenge still remains in finding techniques to relate fabric microstructures to their bulk fluid handling properties, and establishing new methods for combining closure relations to model the effective properties of layered composite materials. Preliminary progress has been made in resolving both these issues.

The authors are supported by EPSRC. (GR/R53890/01). I. E. gratefully acknowledges support from an EPSRC Advanced Fellowship. We also are thankful for support from the Nuffield Foundation, Wellcome Trust and SCA for financial support enabling much of the experimental work to be carried out.

REFERENCES

Abramowitz, M. & Stegun, I. 1964 *Handbook of Mathematical Functions*. National Bureau of Standards, Dover.

Boltzmann, L. 1894 Zur Integration der diffusions Gleichung bei variabeln diffusions Coefficienten. *Ann. Phys.* (*Leipzig*) **53**, 959–964.

Bretherton, F. P. 1961 Slow viscous flow round a cylinder in a simple shear. *J. Fluid Mech.* **12**, 591–613.

Brooks, R. H. & Corey, A. T. 1966 Properties of porous media affecting fluid flow. *Proc. ASCE.* **92**, 61–88.

Celia, M. A., Bouloutas, E. T. & Zarba, R. L. 1990 A general mass-conservative numerical solution for the unsaturated flow equation. *Water Resour. Res.* **26**, 1483–1496.

Chatterjee, P. K. & Gupta, B. S. (Eds.) 2002 *Absorbent Technology*. Textile Science and Technology, vol. 13. Elsevier.

Childs, E. C. & Collis-George, N. 1950 Permeability of porous materials. *Proc. R. Soc. Lond.* A **201**, 392–399.

Darcy, H. 1856 *Les Fountaines Publiques de la Ville de Dijon*. Dalmont, Paris.

Dutkiewicz, J. K. 2003 *Nonwoven Structures for Absorption of Body Fluids*. Edana, Brussels, Belgium.

Eames, I., Small, I., Cottenden, A. & Frampton, A. 2003 Experimental and theoretical study of fluid flow in bed pads. *J. Engng Medicine*. **217**, 263–271.

Gardner, W. R. 1958 Some steady state solutions of the unsaturated moisture flow equations with application to evaporation from a water table. *Soil Sci.* **85**, 228–232.

Gardner, W. R. & Mayhugh, M. S. 1958 Solutions and tests of the diffusion equation for the movement of water in soil. *Proc. Soil Sci. Am.* **22**, 197–201.

Harnett, P. R. & Mehta, P. N. 1984 A survey and comparison of laboratory test methods for measuring wicking. *Textile Res. J.* **54**, 471–478.

Haverkamp, R., Vauclin, M., Touma, J. Wierenga, P. J. & Vachaud, G. 1977 A comparison of numerical simulation models for one-dimensional infiltration. *Soil Sci. Soc. Am. J.* **41**, 285–294.

Hodgson, K. T. & Berg, J. C. 1987 The effect of surfactants on wicking flow in fiber networks. *J. Colloid Interface Sci.* **121**, 22–31.

Hollies, R., Kaessinger, M., Watson, B. & Bogaty, H. 1957 Water transport mechanisms in textile materials Part II: Capillary-type penetration in yarns and fabrics. *Textile Res. J.* **27**, 8–13.

Kirkham, D. & Powers, W. L. 1972 *Advanced Soil Physics*. John Wiley & Sons.

Kissa, E. 1996 Wetting and Wicking. *Textile Res. J.* **66**, 660–668.

Landeryou, M., Yerworth, R. & Cottenden, A. M. 2003 Mapping liquid distribution in absorbent incontinence products. *J. Engng Medicine*. **217**, 253–262.

Miller, B. & Jansen, S. H. 1982 Wicking of liquids in nonwoven fibre assemblies. *Proc. 10th Technical Symp. on Advances in Nonwovens Technology*, November 17–19, pp. 216–226.

Miller, B. & Tyomkin, I. 1994 Liquid porosimetry: new methodology and applications. *J. Colloid Interface Sci.* **162**, 163–170.

Mualem, Y. 1976 A new model for predicting the hydraulic conductivity of unsaturated porous media. *Water Resour. Res.* **12**, 513–522.

Norris, C. & Cottenden, A. 1993 Underpad overview. *Nursing Times* **89**, 26.

Parlange, J. Y. 1971 Theory of water movement in soils, 1. One-dimensional absorption. *Soil Sci.* **111**, 134–137.

Phillip, J. R. 1955 Numerical solution of equations of the diffusion type with diffusivity concentration dependent. *Trans. Faraday Soc.* **51**, 885–892.

Pillai, K. M. & Advani, S. G. 1996 Wicking across a fiber-bank. *J. Colloid Interface Sci.* **183**, 100–110.

Richards, L. A. 1931 Capillary conduction of liquids through porous mediums. *Physics* **1**, 318–333.

Ruoff, A. L., Prince, D. L., Giddings, J. C. & Stewart, G. H. 1959 The diffusion analogy for solvent flow in paper. *Kolloid-Z.* **166**, 144–151.

Russo, D. 1958 Some steady state solutions of unsaturated moisture flow equations with application to evaporation from a water table. *Water Resour. Res.* **24**, 453–459.

van Genuchten, M. Th. 1980 A closed-form equation for predicting the hydraulic conductivity of unsaturated soils. *Soil Sci. Soc. Am. J.* **44**, 892–898.

Washburn, E. W. 1921 The dynamics of capillary flow. *Phys. Rev.* **17**, 273–283.

Witelski, T. P. 2003 Intermediate asymptotics for Richards' equation in a finite layer. *J. Engng Maths* **45**, 379–399.

Youngs, E. G. 1964 An infiltration method of measuring the hydraulic conductivity of unsaturated porous materials. *Soil Sci.* **97**, 307–311.